Transdermal vaccination via 3D-printed microneedles induces potent humoral and cellular immunity

Cassie Caudill[a], Jillian L. Perry[b], Kimon Iliadis[a], Addis T. Tessema[a], Brian J. Lee[c,d], Beverly S. Mecham[a], Shaomin Tian[e,1], and Joseph M. DeSimone[a,b,c,d,1]

[a]Lineberger Comprehensive Cancer Center, University of North Carolina at Chapel Hill, Chapel Hill, NC 27599; [b]Eshelman School of Pharmacy, University of North Carolina at Chapel Hill, Chapel Hill, NC 27599; [c]Department of Radiology, Stanford University, Stanford, CA 94305; [d]Department of Chemical Engineering, Stanford University, Stanford, CA 94305; and [e]Department of Microbiology and Immunology, University of North Carolina at Chapel Hill, Chapel Hill, NC 27599

Edited by Darrell J. Irvine, Massachusetts Institute of Technology, Cambridge, MA, and accepted by Editorial Board Member Joanna Aizenberg August 17, 2021 (received for review February 8, 2021)

Vaccination is an essential public health measure for infectious disease prevention. The exposure of the immune system to vaccine formulations with the appropriate kinetics is critical for inducing protective immunity. In this work, faceted microneedle arrays were designed and fabricated utilizing a three-dimensional (3D)-printing technique called continuous liquid interface production (CLIP). The faceted microneedle design resulted in increased surface area as compared with the smooth square pyramidal design, ultimately leading to enhanced surface coating of model vaccine components (ovalbumin and CpG). Utilizing fluorescent tags and live-animal imaging, we evaluated in vivo cargo retention and bioavailability in mice as a function of route of delivery. Compared with subcutaneous bolus injection of the soluble components, microneedle transdermal delivery not only resulted in enhanced cargo retention in the skin but also improved immune cell activation in the draining lymph nodes. Furthermore, the microneedle vaccine induced a potent humoral immune response, with higher total IgG (Immunoglobulin G) and a more balanced IgG1/IgG2a repertoire and achieved dose sparing. Furthermore, it elicited T cell responses as characterized by functional cytotoxic $CD8^+$ T cells and $CD4^+$ T cells secreting Th1 (T helper type 1)-cytokines. Taken together, CLIP 3D–printed microneedles coated with vaccine components provide a useful platform for a noninvasive, self-applicable vaccination.

microneedles | 3D printing | continuous liquid interface production | vaccine | transdermal delivery

Vaccines play a vital role in global healthcare. Prophylactic vaccines have nearly eliminated diseases such as smallpox and measles and have the potential to curb many other common infectious diseases as well as emerging epidemics (Ebola) and pandemics (COVID-19). Vaccines are formulated to deliver target antigens to the immune system in order to generate potent and durable protective immune responses against pathogens and prevent future infections. Subunit vaccines consisting of purified antigens are a major focus of modern prophylactic vaccine development due to their much-improved safety profile than the live attenuated and inactivated vaccines (1). However, subunit vaccines are generally not as immunogenic as whole pathogen-based vaccines because of the lack of immunostimulatory components and/or inefficient detection by the immune system. The addition of immunostimulatory agents (adjuvants) (2, 3) and customized delivery vehicles (like particles and microneedles) have shown great promise in improving the efficacy of subunit vaccines (4, 5).

Effective vaccines generally need to deliver antigens and adjuvants to the right set of innate immune cells, such as dendritic cells (DCs) and macrophages, to facilitate antigen presentation, T cell priming, and the formation of memory T cells and B cells as well as antibody-secreting plasma cells (6). Accumulating evidence suggests that vaccine kinetics and location of delivery play an essential role in promoting protective immunity while keeping the adverse effects under control (7). We have previously shown that the formation of an antigen depot and sustained cargo release at the injection site, as well as an extended presence of antigen in the draining lymph nodes via nanoparticle delivery, greatly improved humoral immunity (8, 9). Furthermore, the route of vaccine administration can potentially impact the performance of a vaccine formulation. While vaccines are typically administered as bolus injections into the muscle or subcutaneous space, there is increasing interest in the intradermal (ID) route, as human skin is rich in immune cells (Langerhans cells and dermal DCs) (10). ID vaccination has demonstrated improved vaccine efficacy with dose sparing (11–13); however, ID injections require trained medical personnel, are painful, and are difficult to administer, requiring development of new ID devices (14). Leveraging these learnings, we aimed to develop a subunit vaccine to provide sustained delivery of both antigens and adjuvants in the skin, utilizing microneedles for ID delivery.

Microneedles (MNs) are arrays of micrometer-sized solid needle projections that can painlessly puncture the stratum corneum and deliver therapeutics into the epidermis/dermis. MNs can be fabricated out of solid metal, silicon, or polymers and are coated with therapeutics or fabricated out of degradable materials that encapsulate therapeutics (15–17). Once applied to the skin, the cargo either

Significance

Vaccination is essential for combatting emerging epidemics and pandemics. Microneedle patches designed to precisely deliver cargos into the intradermal space, rich in immune cells, provide a noninvasive and self-applicable vaccination approach, eliminating the need for hypodermic needles and trained medical personnel for vaccine administration. Here, we show that advanced 3D printing methods allow for the manufacturing of polymeric microneedles of controlled geometries (difficult to manufacture using traditional methods) designed to enhance vaccine component coating. Using model vaccine components, we demonstrated that 3D-printed microneedle delivery resulted in enhanced cargo retention in the skin, activation of immune cells, and more potent humoral and cellular immune responses as compared with traditional vaccination routes.

Author contributions: C.C., J.L.P., B.S.M., S.T., and J.M.D. designed research; C.C., J.L.P., K.I., A.T.T., and S.T. performed research; A.T.T. and B.J.L. contributed new reagents/analytic tools; C.C., J.L.P., K.I., B.J.L., and S.T. analyzed data; and J.L.P., S.T., and J.M.D. wrote the paper.

Competing interest statement: J.M.D. has an equity stake in Carbon, Inc, which is a venture-backed manufacturer of CLIP 3D–printing equipment.

This article is a PNAS Direct Submission. D.J.I. is a guest editor invited by the Editorial Board.

[1]To whom correspondence may be addressed. Email: shmtian@med.unc.edu or jmdesimone@stanford.edu.

This article contains supporting information online at https://www.pnas.org/lookup/suppl/doi:10.1073/pnas.2102595118/-/DCSupplemental.

Published September 22, 2021.

dissolves off the MNs, or the MN matrix material degrades and releases the cargo into the skin. Much work has been done in the field, characterizing methods for MN drug delivery through either developing methods for coating solid microneedles with cargo (18–21) or evaluating degradable polymer matrices for transdermal drug delivery (22–26).

Parenteral vaccine delivery to the skin via MNs has been actively explored in the last decade (11, 18, 22, 24–29). MN vaccination is simple, lending itself to self-administration, and eliminates the need for trained medical personnel and hypodermic needles. Furthermore, the MN design inherently targets the cargo to the ID space, and MN vaccines have demonstrated dose sparing as well as improved protection as compared with hypodermic injections (30). Beyond the point-of-use benefits and enhanced vaccine protection, MN vaccines are formulated and stored in a dried form, eliminating the need for vaccine reconstitution and potentially reducing or eliminating the cold supply chain (23, 31–34).

Current methods for making MNs arrays have their foundation in the fabrication techniques associated with the microelectronics industry. MNs can either be made directly by microfabrication techniques or indirectly by first fabricating master templates using microfabrication techniques and then making molds, or relief patterns, using soft lithographic techniques, which are used to mold the microneedles out of a range of materials. The template fabrication and molding process enables control over the size and shape of the MNs; however, there are significant drawbacks with this indirect fabrication approach. First, many desirable needle geometries can be challenging to make by microfabrication techniques, like needles of different sizes and shapes on the same patch (to avoid the bed-of-nails effect) or needles with undercuts to create high surface areas which are unmoldable. Second, needle sharpness is often diminished after repeated molding, leading to loss of replication fidelity. Third, for molded microneedles, one needs to tie the mechanical properties of the formulation chemistries to the mechanical properties associated with insertion into the skin, which can be a challenge. Arguably, the field of microneedles needs a breakthrough in fabrication approaches to fully unlock the potential of microneedles to address a number of drug and vaccine delivery needs.

Additive manufacturing (three-dimensional [3D] printing) has recently emerged as a microneedle fabrication technology; however, due to resolution limitations, there are very few instances in the literature in which MN patches can be directly 3D printed and used in vivo for transdermal delivery. We have previously demonstrated that utilizing continuous liquid interface production (CLIP) 3D-printing technology, MNs with tunable geometries can be rapidly printed (in the range of minutes) (35), coated with biologics, and used to deliver cargos transdermally in mice (21). Herein, we report the fabrication of faceted microneedles made by CLIP-based 3D printing, designed to increase the surface area of the microneedles to increase the amount of vaccine cargo that can be coated on a given area of the MN patch. In comparison with the square pyramidal microneedle design, the faceted MN array design yielded enhanced surface coatings of model vaccine components (ovalbumin and CpG). Utilizing fluorescent tags and in vivo imaging system (IVIS), we evaluated cargo delivery and retention in mice as a function of route of delivery, either subcutaneous bolus injection of the soluble components or microneedle transdermal delivery. We observed that, compared with the subcutaneous injection of soluble components, MN delivery not only enhanced the cargo retention in the skin and the activation of immune cells in the draining lymph nodes (dLNs) but also induced more potent Th1-biased humoral and cellular immune responses.

Results

Design and Fabrication of Faceted MNs by CLIP. CLIP 3D–printing technology enables high precision and consistency in size, shape, and spacing of every needle in an array (35). Previously, we have reported printing square pyramidal MNs out of polyethylene glycol dimethacrylate (M_n = 350) ($PEG_{350}DMA$), which provides high strength for skin penetration (21). In this study, 700 μm PEG MNs were printed in a 10 × 10 array on a 10 × 10 mm patch for vaccine delivery. In addition to the common square pyramidal design, a faceted MN with horizontal grooves was designed to increase surface area and cargo loading (Fig. 1*A*). Both square pyramidal and faceted MNs remained intact after coating with a model antigen ovalbumin (OVA) formulated in a viscous water-based coating solution including 3.4 weight (wt)% methylcellulose or sodium alginate, 21 wt% sucrose, and 7 wt% OVA (Fig. 1*A* and *SI Appendix*, Fig. S1*A*). We observed an average (as a compilation of four individual coating experiments, with n = 4/5 microneedles per coating, *SI Appendix*, Fig. S2) loading of 27.6 and 20.3 μg OVA per patch for the faceted and square pyramidal microneedles respectively (Fig. 1*B*). Thus, by increasing the surface area, we were able to achieve a 36% higher OVA loading. As the theoretical increase in surface area is only 21.3%, it is likely that the geometry of faceted MN may allow thicker coating than the square pyramidal MNs in certain areas.

Loading of Antigen and Adjuvant onto Microneedle Patches. Vaccine formulations generally consist of multiple components. In order to codeliver vaccine antigen(s) and adjuvant(s), we coated MNs with a model vaccine formulation including OVA, a model antigen, and CpG oligonucleotide, a Toll-like receptor 9 agonist and potent immunostimulator. All microneedle vaccines were coated with cargo-utilizing 3D-printed coating masks (21). Simply, the microneedle patches were inserted (one patch at a time) into the solution-filled coating mask, held for 10 s, and then removed and allowed to air dry, resulting in cargo-coated microneedles (one coating only). Microneedles were either coloaded with the OVA and CpG mixture onto the same microneedles (nonsectional coating) or coated with OVA and CpG on separate needles within a single patch (sectional coating). For sectional coating, the mask was partitioned such that 30 wells were filled with a coating solution containing OVA and 70 wells with a coating solution containing CpG (Fig. 1*C*). Fig. 1 *D* and *E* show a representative photograph and fluorescence image of a faceted MN patch sectionally coated with OVA–Texas Red and fluorescein isothiocyanate CpG1826 conjugate (CpG-FITC). Both methods of loading resulted in ~17 μg OVA and 2.5 μg CpG (*SI Appendix*, Fig. S3), a relevant starting point for inducing immune responses in mice. These loading amounts can be easily tuned by adjusting the coating mask sections or cargo concentrations. In addition, the current coating formulation allows relatively fast cargo release in aqueous solutions, with >80% OVA and CpG released in 2 h (*SI Appendix*, Fig. S1*B*).

Transdermal Delivery of Antigen and Adjuvant Via MN Patches. To evaluate how MNs work in delivering vaccine components in vivo, we compared cargo delivery by MNs and soluble OVA + CpG delivered by standard subcutaneous (SC) injection methods in mice over 72 h. In order to track cargo in mouse skin, OVA and CpG labeled with Texas Red and FITC, respectively, were visualized using the IVIS Lumina at two fluorescence channels. As shown in *SI Appendix*, Fig. S4, cargo fluorescence can be seen after 2 min of MN skin application as well as the skin indentations left by needle penetration. By comparing cargo fluorescence before and after skin application, delivery efficiency was calculated. CpG MN delivery to the skin was slightly more efficient than OVA, 80% versus 70% within 2 h, likely due to its lower molecular weight (Fig. 2*A*). The cargo fluorescence in the skin was further tracked by IVIS imaging over 72 h. MN-mediated CpG delivery showed significantly longer persistence at the application site (detectable up to 72 h) than SC-injected CpG (detectable up to 24 h) (Fig. 2*B* and quantified in Fig. 2*D*). In the contrast, there was no significant difference between MN and SC groups in OVA delivery (Fig. 2 *C* and *E*).

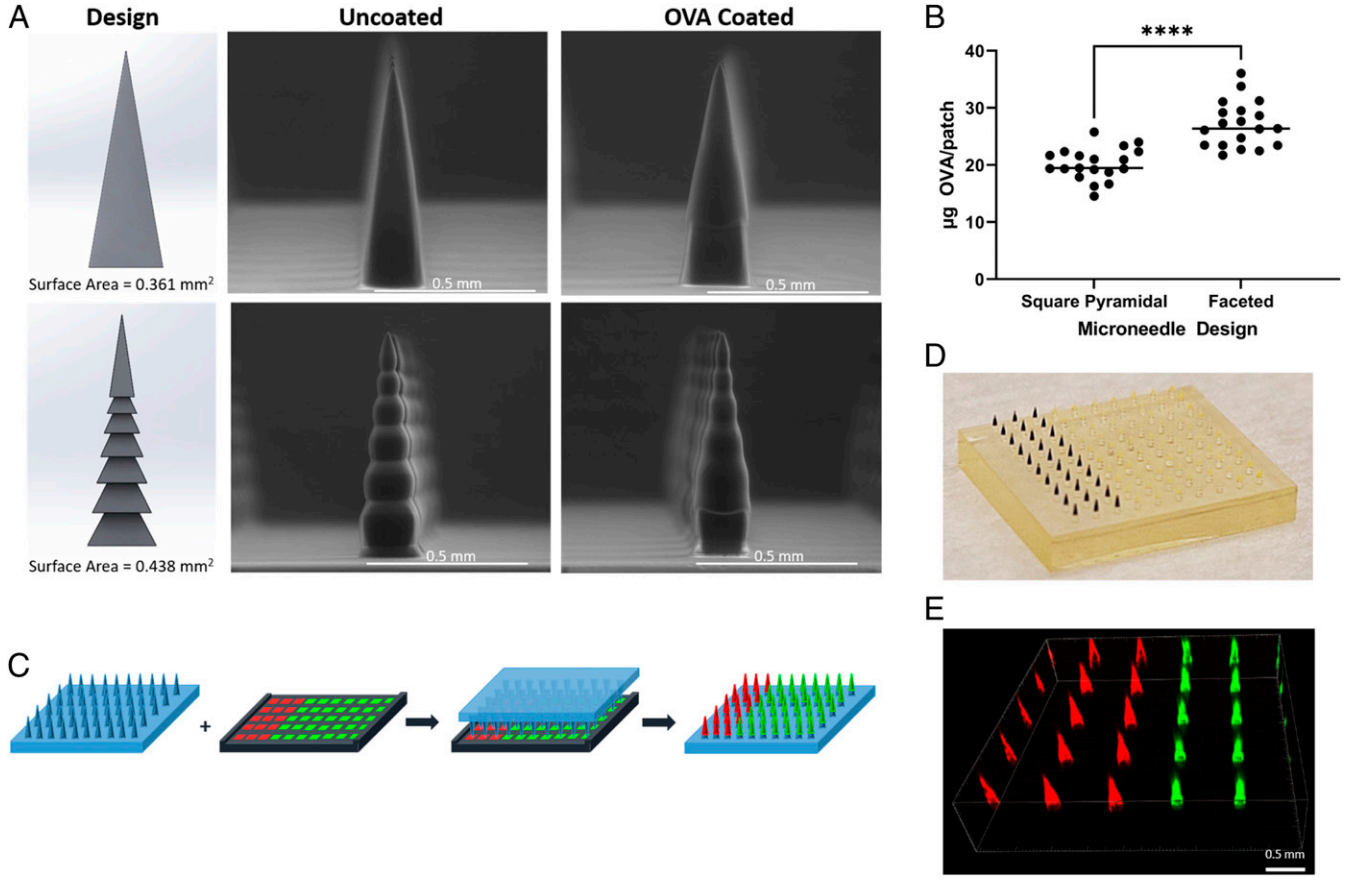

Fig. 1. CLIP-printed MNs for vaccine formulation. (*A*) Design and environmental scanning electron microscope (ESEM) images. (*Top*) Square pyramidal MN. (*Bottom*) Faceted MN. (*B*) Ovalbumin coating ($n = 19$). Data are presented as mean ± SD of individual samples, statistical analysis by unpaired Student's *t* tests. ****$P < 0.0001$. (*C*) Cargo co-coating scheme. A matching coating mask was used to simultaneously load two cargos onto two sections of needle array. (*C*) Ovalbumin coating ($n = 19$). Data are presented as mean ± SD of individual samples, statistical analysis by unpaired Student's *t* tests. ****$P < 0.0001$. (*D*) Photograph of an OVA–Texas Red and CpG-FITC co-coated MN patch. (*E*) Fluorescence image of the MN patch in *D*.

Cargo Availability in the dLNs and Activation of Immune Cells. Lymph nodes are the primary peripheral lymphoid organs for the generation of vaccine-induced adaptive immunity. Therefore, we further examined the availability of fluorescently labeled cargos in the dLNs and the immune cell activation in the dLNs. CpG-FITC delivered by MN showed higher accumulation in dLNs than SC at 72 h (Fig. 3*A*), while the accumulation of MN-delivered OVA–Texas Red in dLNs was significantly higher than SC at 24 h (Fig. 3*B*). The MN vaccine was also much more efficient in recruiting immune cells into the dLNs as indicated by not only the total cellularity of dLNs over 72 h posttreatment (Fig. 3*C*) but also the individual immune cell types, like DCs (Fig. 3*D*), macrophages, T cells, pDCs, and B cells (*SI Appendix*, Fig. S5 *A–E*). Furthermore, the MN vaccine was able to more efficiently induce immune cell activation and maturation of antigen-presenting cells (APCs) as indicated by higher expression of the costimulatory marker CD80 (Fig. 3*E* and *SI Appendix*, Fig. S5 *F–I*). Overall, the MN vaccine formulation is very potent in activating dLNs and getting them ready for the generation of an adaptive immune response.

Potent Humoral and Cellular Immune Responses to the MN Vaccine in Mice. To assess the immune response induced by MN vaccines, C57BL/6 mice were immunized on day 0 and boosted on day 23, receiving 16.5 μg OVA and 2.5 μg CpG for each immunization. MN patches were applied with thumb pressure for 2 min and then bandaged and left in the skin for 24 h before removal. Control groups included untreated, uncoated blank MNs, SC and ID injections of soluble OVA+CpG and Alum + OVA. Compared with SC and ID routes of delivery of soluble OVA+CpG, transdermal delivery by the MN vaccine induced a 20 times higher OVA-specific IgG response after the prime immunization (day 21, *SI Appendix*, Fig. S6) and a 50 times higher response after the boost immunization (day 30, Fig. 4*A*), a response that was comparable to the benchmark adjuvant Alum-based formulation. Furthermore, both sectionally and nonsectionally coated MN vaccine patches were able to elicit a similarly strong IgG response (*SI Appendix*, Fig. S7).

Alum promoted Th2-biased immunity as shown by the high levels of IgG1 (Fig. 4*B*) and the minimum levels of IgG2a (which represent Th1 type immunity) (Fig. 4*C*); this observation in IgG isotype switching is consistent with literature results (36). In contrast, CpG is an adjuvant that drives Th1-biased immunity (37). As shown in Fig. 4 *B* and *C*, ID delivery of antigen and CpG via the MN vaccine and ID vaccination were able to elicit both IgG2a and IgG1, therefore more balanced subclasses of IgG. Strikingly, the same formulation of OVA and CpG administered subcutaneously did not induce detectable IgG2a, suggesting that vaccine delivery into the skin favors Th1-biased immunity. To generate high-affinity antibodies, antigen-activated B cells need to enter germinal centers (GC), a specialized structure in the secondary lymphoid organs, to undergo affinity maturation of their antigen receptors and then differentiate into either long-lived antibody-secreting plasma cells or memory B cells that are crucial for long-term protection. Fig. 4*D* shows that by day 46, immunization with the MN vaccine increased total GC B cells in the dLNs by about twofold compared with OVA+CpG ID and SC routes or Alum+OVA SC.

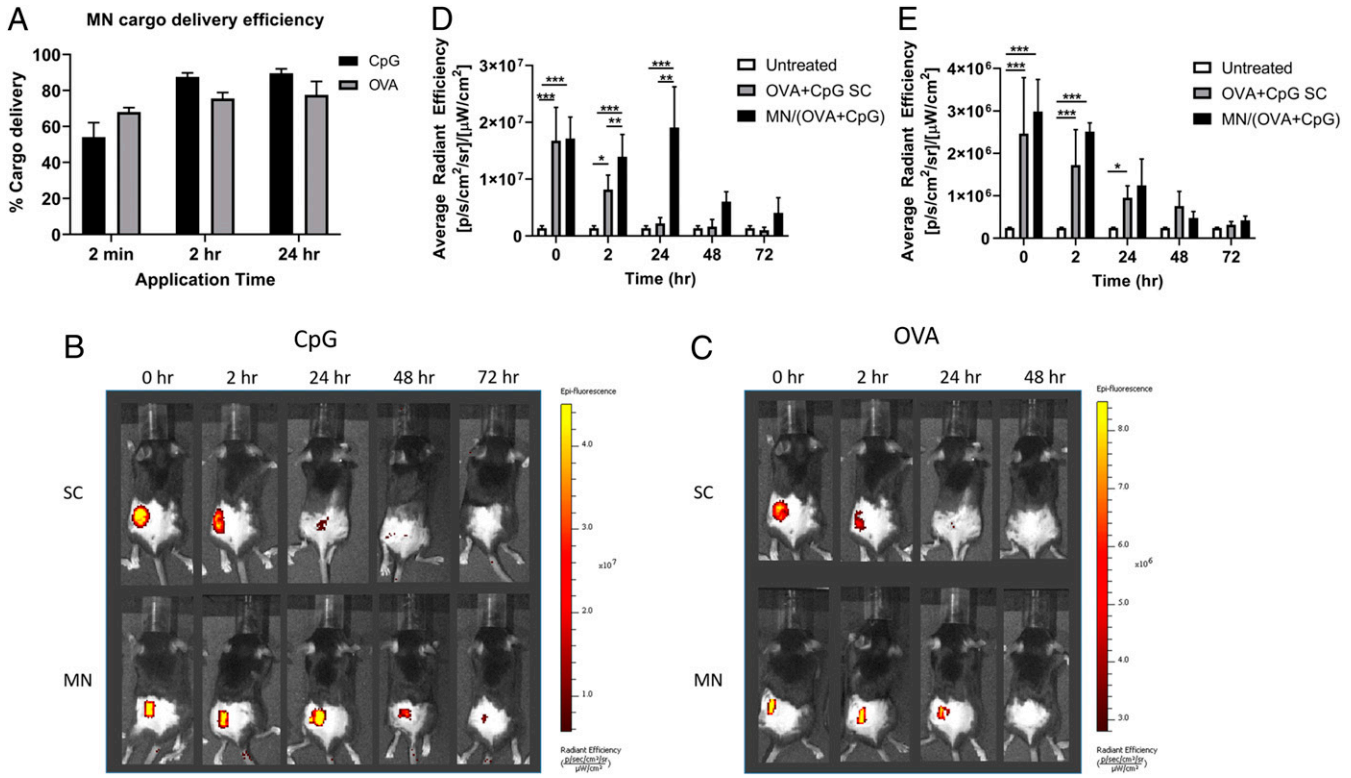

Fig. 2. Transdermal cargo delivery by sectionally coated MN patches. Mice were either treated with OVA + CpG on MN patches or through SC delivery of soluble cargos. (*A*) Cargo delivery efficiency was calculated for sectionally coated MN patches after 2 min, 2, or 24 h application time. Cargo retention at the delivery site was evaluated at the indicated time points following cargo delivery via IVIS live-animal imaging to track (*B*) CpG or (*C*) OVA at the delivery site over time. (*D*) CpG fluorescence quantified from images in *B*. (*E*) OVA fluorescence quantified from *C*. Data are presented as mean ± SD of samples from individual animals ($n = 4$ for each group). Statistical analysis was done by one-way ANOVA. $^*P < 0.05$, $^{**}P < 0.01$, $^{***}P < 0.001$.

In addition to the potent broad humoral immunity, dose sparing was also achieved by the MN vaccine formulation (Fig. 4*E*). MN vaccines with 16.7 μg OVA and 2.5 μg CpG induced a comparable level of humoral responses as a MN vaccine with 1.3 μg OVA and 2.5 μg CpG (not significantly different). Similarly, reducing CpG by five times did not significantly decrease the level of humoral responses. This not only makes a more cost-effective vaccination available but also helps to limit the potential antigen or adjuvant-induced side effects. A similar dose-sparing effect was observed with intramuscular injections but not with the subcutaneous or ID vaccinations. On the other hand, at each antigen and adjuvant dosage level, the MN vaccine outperformed all routes of administration (ID, SC, and intramuscular) in the elicitation of humoral immunity (Fig. 4*E*).

Lastly, we examined the duration of the MN vaccine–induced antibody response (Fig. 4*F*). The MN vaccine–induced IgG response peaked around day 49, decreased over time, and plateaued after day 147. The response was still detectable by day 196, while the OVA+CpG SC–induced response returned to baseline by day 119. The Alum-adjuvanted formulation, on the other hand, was able to elicit a more durable antibody response. Together, these data suggest that this MN-based vaccine formulation is very effective in promoting an antigen-specific humoral response.

While the majority of prophylactic vaccines are thought to function through the induction of protective antibodies, T cell–mediated immunity also plays a critical role against chronic viral infections like human immunodeficiency virus (HIV) and hepatitis C virus (38). Here, we show that MN-based skin delivery of OVA and CpG was able to induce Th1-biased $CD4^+$ helper T cell and $CD8^+$ cytotoxic T cell responses against OVA. After restimulation with OVA257-264 (SIINFEKL), a dominant OVA T cell epitope, the frequency of $CD8^+$ T cells producing effector cytokine IFN-γ in response to the MN vaccine was twofold higher than that in response to the ID injection of OVA+CpG (Fig. 5*A*). On the other hand, SC vaccination induced minimum IFN-γ–producing $CD8^+$ T cells. $CD4^+$ T responses after restimulation with OVA were biased toward secretion of Th1 cytokines IFN-γ and IL-2 for MN, SC, and ID vaccinations, while Alum+OVA SC was more potent inducing IL-2, the cytokine enhancing T cell proliferation. Th1 cytokine TNF and Th2 cytokine IL-4 were also assayed, but a detectable signal was not observed across the groups. Overall, MN-based vaccination in the skin can efficiently elicit T cell immunity with a bias toward Th1 response, which is consistent with the observation that the MN vaccine was potent in activating DCs (Fig. 3 *D* and *E*), which are important in priming T cells.

Discussion

MN-based transdermal/ID vaccine delivery to the skin provides many benefits over traditional vaccines, including noninvasiveness and less tissue damage, self-applicability, potential to minimize dependence on the cold chain, and reduced needs for professional administration of hypodermic needles (11). Therefore, the formulation of MN vaccines has a paramount potential to expand global immunization capabilities to not only meet regular vaccination needs but to also respond faster to epidemics and pandemics like COVID-19 (39). Being a mold-less MN technology, CLIP 3D printing technology enables direct fabrication of MNs via photopolymerization of liquid resin into a form designated by a computer-aided design (CAD) file (35). This allows the direct fabrication and rapid screening of a multitude of MN properties (geometry, composition, density, etc.) in an iterative design process,

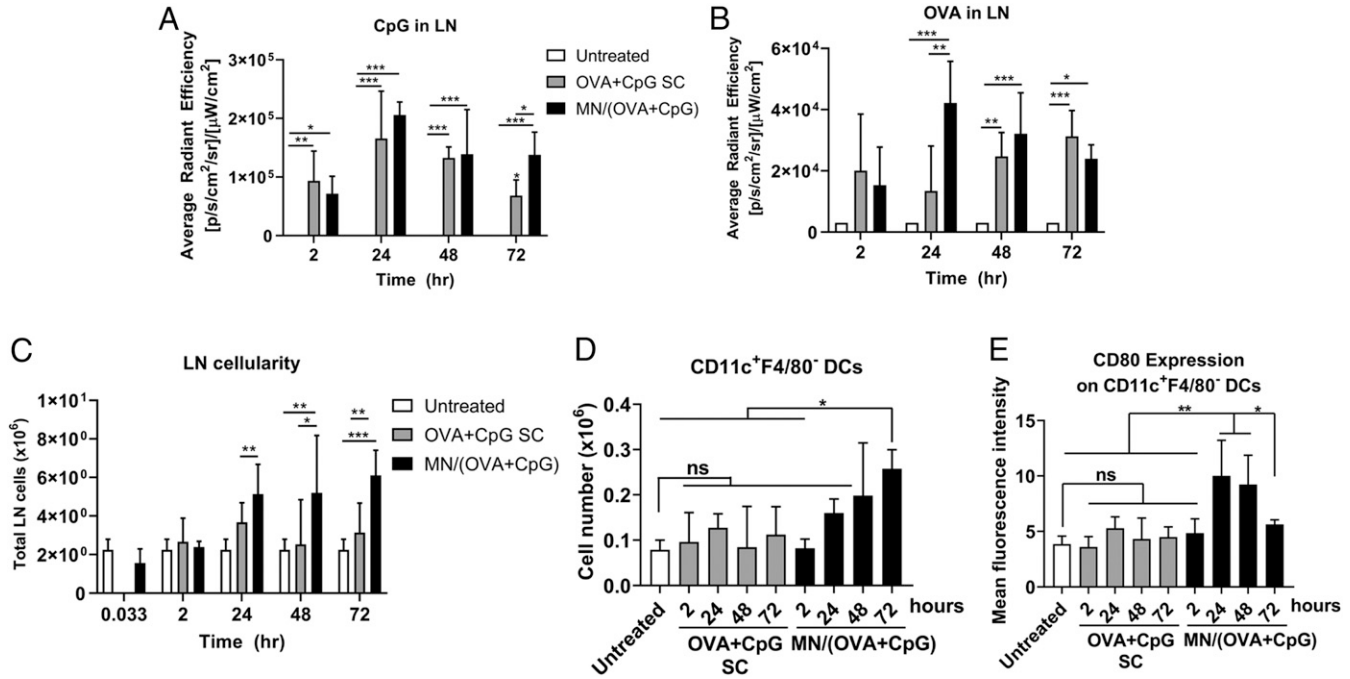

Fig. 3. Cargo drainage to lymph nodes (LNs) and activation of LN cells. The draining inguinal LNs from mice (the same animals as in Fig. 2) were harvested and imaged for cargo fluorescence by IVIS. (*A*) CpG fluorescence in dLNs and (*B*) OVA fluorescence in dLNs. Dissociated LN cells were then counted and further stained with antibodies for cell markers followed by flow cytometry analysis. (*C*) Cellularity of dLNs. (*D*) Number of dendritic cells in dLNs. (*E*) Expression of costimulatory molecule CD80 on dendritic cells in dLNs. Data are presented as mean ± SD of samples from individual animals ($n = 4$ for all groups). Statistical analysis by one-way ANOVA. $*P < 0.05$, $**P < 0.01$, $***P < 0.001$. ns, not significant.

without the need to consider parameters associated with mold filling or the limitations of needle geometries that cannot be molded.

In this study, a faceted polymeric MN was designed and 3D printed by CLIP technology for vaccine formulation and transdermal delivery. Compared with smooth square pyramidal MNs, the increased surface area of faceted MNs can significantly enhance cargo loading via surface coating, which is a relatively gentle process that is suitable for the loading of biologics. Furthermore, the utilization of a specially designed coating mask previously developed (21) allowed us to co-load multiple cargos in specified sections of the MN array. We expect that such a loading strategy would further allow for the combination of multiple antigens (like proteins, RNAs, and DNAs) and adjuvants with different chemical structures that may be chemically incompatible.

We have demonstrated that transdermal delivery of a model vaccine formulation by MNs is superior to subcutaneously or intradermally administered soluble formulation in eliciting potent antibody responses in both initial antigen-specific IgG and the duration of the response. This could be attributed to more efficient and sustained availability of antigen/adjuvant via MN transdermal delivery in the dermal space as well as in the draining lymph nodes where adaptive immunity develops. The viscous coating formulation could also contribute to the slower clearance of cargos. Sustained cargo availability not only favors antigen presentation but also enhances the function of adjuvants that activates innate immune responses to create a local immunocompetent environment at both injection site and dLNs (40).

Adjuvants have been widely explored to help boost the immunogenicity of purified subunit antigens and shape vaccine protection (2). For example, Alum, the benchmark adjuvant with the longest and most widespread clinical usage, elicits Th2-biased immunity (development of Th2 $CD4^+$ helper T cells, IgG1 subclass dominant, and minimum cytotoxic $CD8^+$ T cells) (36). While there is generally a lack of detailed understanding about what types of immune responses are effective at preventing infection, the development of novel adjuvants has aimed to activate different parts of innate and adaptive immunity to achieve more balanced immunity for fighting against various infectious diseases. We have adopted a CpG oligo as a vaccine adjuvant, which stimulates strong Th1-biased immune responses (37) and has been approved in Dynavax Technologies's US hepatitis B vaccine and tested in many other preclinical and clinical vaccine studies (41, 42). As expected, the addition of CpG induced more balanced IgG subclasses and Th1-biased T cell responses, but interestingly, this was only observed for the MN vaccine and not the subcutaneously injected soluble formulation. This result suggests that the delivery of the adjuvant to the right dermal space and innate immune cells could be essential for the adjuvant to drive the desired immunity.

Our MN model vaccine elicited a comparable antibody response to the Alum-adjuvanted formulation upon vaccination, although the humoral response did not last as long as the Alum vaccine formulation. This result is not surprising, as Alum not only acts as an irritant to promote inflammatory responses but also exists in a particle form that facilitates the formation of an antigen depot, which favors sustained availability of antigens (40). Therefore, one of the ongoing efforts in improving the 3D-printed MN vaccine is to design biodegradable MNs affixed to a removable backing, allowing the MNs to stay in the ID space, slowly releasing the vaccine cargos to achieve the depot effect associated with Alum-adjuvanted vaccine formulations. Indeed, enhanced humoral immunity has been reported for implantable MN patch vaccination that provided sustained cargo release (22, 24). Other strategies to improve cellular responses are also being explored, for example, the incorporation of cargos encapsulated in virus-mimicking nanoparticles or the utilization of materials that dissolve/degrade into particles in order to facilitate intracellular delivery of antigens as inspired by MN-based vaccines integrating live antigen–expressing viral vectors, messenger RNA, or inactivated viruses (29, 33, 39, 43).

In summary, we have designed and fabricated a faceted MN array via CLIP 3D printing and established an approach to co-load

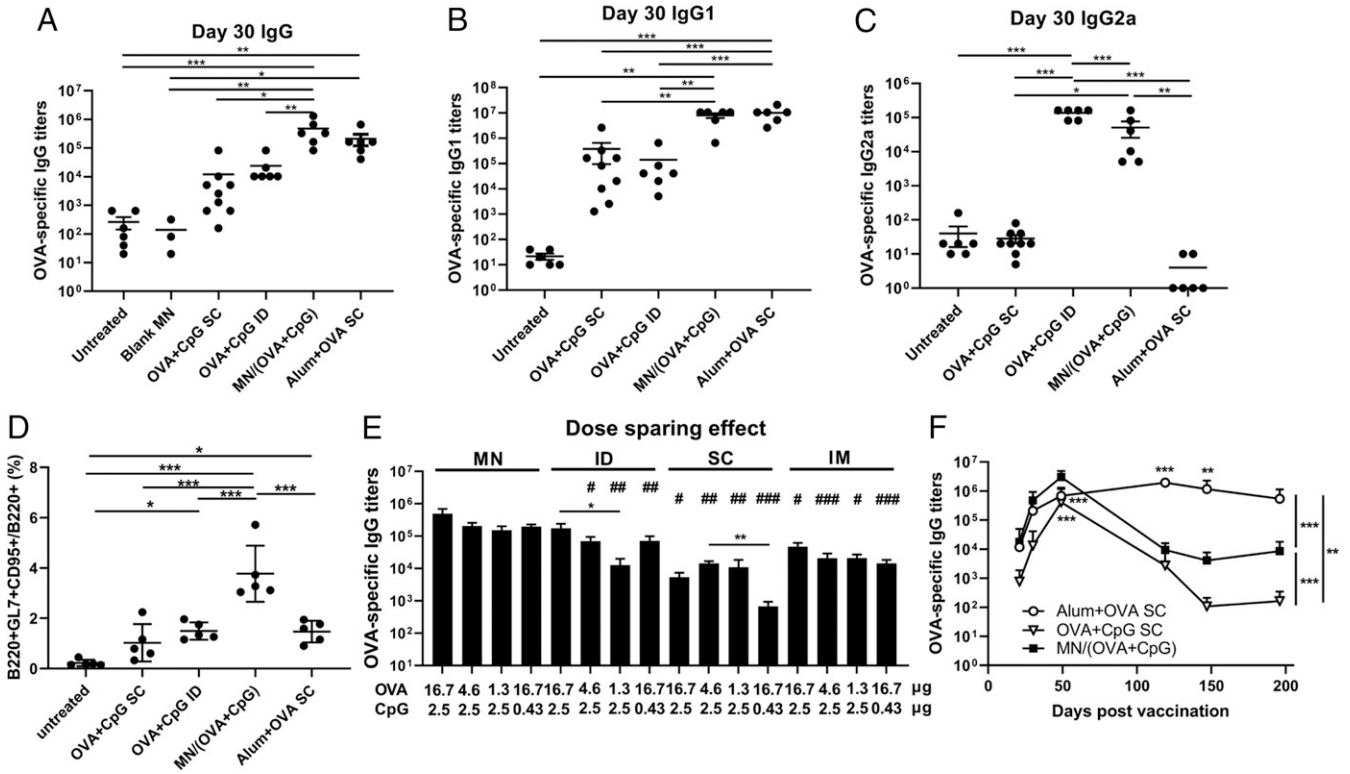

Fig. 4. MN vaccine induces potent humoral immune responses. Mice were either untreated ($n = 6$) or immunized with blank MN ($n = 3$), OVA (16.7 μg) + CpG (2.5 μg) –coated MN patches ($n = 6$), OVA (16.7 μg) + CpG (2.5 μg) subcutaneously injected ($n = 9$) or intradermally injected ($n = 6$), or SC injection of 500 μg Alum + 16.7 μg OVA ($n = 6$). All groups received two immunizations of the same doses of antigen and adjuvant on day 0 and 23. Serum samples were collected on day 21, 30, 49, 119, 147, and 196 and analyzed by ELISA. (*A*) Total IgG on day 30. (*B*) IgG1 on Day 30. (*C*) IgG2a on day 30. (*D*) Percentage of B cells in GCs in the dLNs on day 46 post–prime immunization by flow cytometry analysis. For the dose-sparing study, mice were immunized ($n = 5$ per group) on days 0 and 21 with MN patches loaded with various amounts of OVA and CpG or the equivalent of soluble OVA and CpG injected by ID, SC, or intramuscular (IM) routes. OVA-specific IgG titers were evaluated on day 28 (*E*). (*F*) Kinetics of IgG. All data are presented as mean ± SD of samples of individual animals. For *A*–*E*, data were analyzed by one-way ANOVA. In *E*, the data were analyzed by one-way ANOVA within each administration route (shown as *) or across the groups among the various routes with equivalent dosages (shown as #, all against MN). In *F*, data were compared by two-way ANOVA. * and #, $P < 0.05$; ** and ##, $P < 0.01$; *** and ###, $P < 0.001$.

multiple vaccine components with high tunability. Our model vaccine demonstrated efficient ID delivery of vaccine components as well as the induction of potent and balanced humoral and cellular immunity. The combination of fast 3D-printing technology with MN vaccine formulation could provide a versatile platform to improve global immunization and healthcare.

Materials and Methods

Materials. Diphenyl(2,4,6-trimethylbenzoyl)phosphine oxide (TPO), sucrose, methylcellulose (Mw = 17,000 Da), sodium alginate, CpG1826, and CpG-FITC were purchased from Sigma-Aldrich. $PEG_{350}DMA$ was obtained from TCI America. EndoGrade endotoxin-free ovalbumin (<0.1 EU/mg) was from Hyglos. OVA–Texas Red was from Invitrogen. Fluorescent-labeled antibodies for flow cytometry

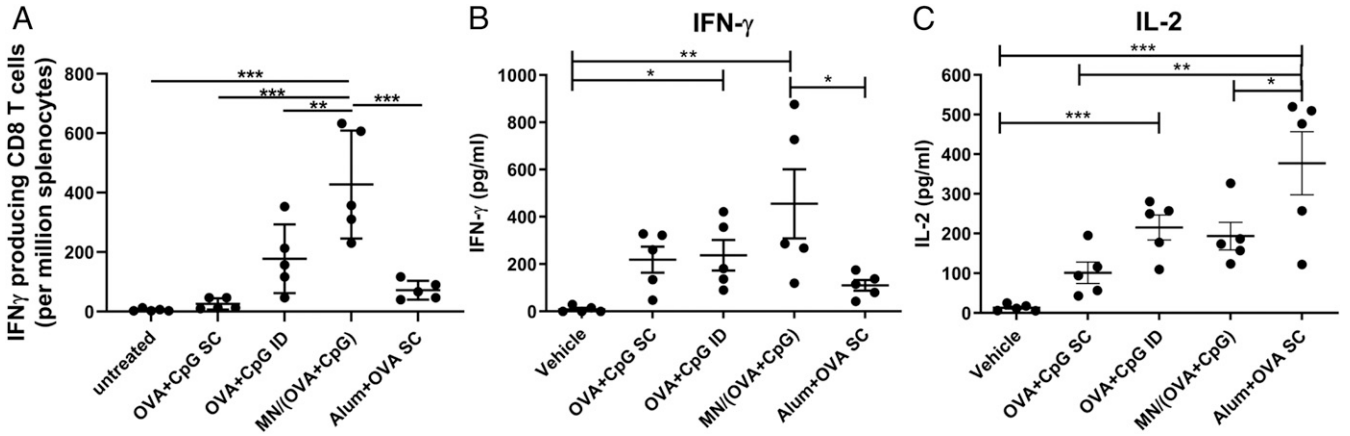

Fig. 5. T cell activation by MN vaccine. Spleens from the immunized mice (same as in Fig. 4 *A*–*D*) were analyzed for (*A*) IFN-γ–producing CD8 T cells by ELISpot and (*B* and *C*) Cytokine production in CD4 T cells by ELISA. Data are presented as mean ± SD of samples from individual animals, with statistical analysis by one-way ANOVA. *$P < 0.05$, **$P < 0.01$, ***$P < 0.001$.

were from eBiosciences. Horseradish peroxidase (HRP)-conjugated goat anti-mouse IgG, IgG1, and IgG2a were from Santa Cruz.

Fabrication of MN Patches and Coating Masks. MN patches and coating masks were 3D printed using an S1 CLIP prototype printer (Carbon) as previously reported (21). Briefly, CAD files of MN patches and coating mask devices were produced using SolidWorks 2014. MNs were square pyramidal shaped or faceted and 700-μm tall and 233-μm wide at the base. MN patches consisted of an array of 10 × 10 needles with 500-μm spacing between needles on an 8.8 × 7.8 × 1 mm base. Coating mask devices consisted of a 10 × 10 array of 275 × 275 μm wells in an 8.8 × 7.8 × 0.5 mm plate, with a reservoir under the plate for the coating solution. Raised edges between 150 μm in height were placed on the surface of the coating mask. Both MNs and coating mask devices were fabricated from a resin composed of $PEG_{350}DMA$ with 2.5 wt% TPO as a photoinitiator. MNs and coating masks were printed with a 1-μm slice thickness, speed of 12 mm/hour, and 4 and 1 mW/cm^2 light intensity (λ = 385 nm), respectively. After fabrication, MNs and coating masks were briefly rinsed with isopropanol to remove residual resin and postcured for 5 min using a Phoseon FireJet FJ800 ultraviolet light emitting diode (LED) lamp.

Cargo Loading and Quantification. MN coating solutions were prepared by first dissolving 30 mg methylcellulose or sodium alginate in 1 mL water with stirring at 85 °C for 1 h and then incubating at 4 °C overnight. A total of 300 mg sucrose was mixed in and shaken at room temperature for 30 min until dissolved. OVA or CpG were then added to the coating solution at 7 and 1.2 wt% and shaken at room temperature for around 30 min until dissolved. To coat the MNs, coating mask devices were attached to a sterile Petri dish surface with double-sided tape and filled with 100 μL coating solution. MN patches were inserted one time into the coating mask device, held in the device for ∼10 seconds, and then removed and allowed to air dry at room temperature for 1 h. For sectional coating, coating masks with two-compartment reservoirs were printed as above, and each reservoir filled with coating solutions containing either 7 wt% OVA (or OVA–Texas Red) or 1.2 wt% CpG (or CpG-FITC). To quantify cargo loading, coated MN patches (n = 4 to 5) were incubated in 150 μL phosphate-buffered saline for 2 h at room temperature. Released protein was analyzed by bicinchoninic acid (BCA) assay, and CpG was quantified by absorbance at 260 nm.

Animals. Female C57BL/6 mice were purchased from Jackson Laboratory and used for transdermal cargo delivery and immunization studies at 6 to 12 wk of age. All mouse experiments were performed under protocols approved by the Institutional Animal Care and Use committee of the University of North Carolina. All experiments followed ethical and federal regulations according to the Public Health Service Policy on Humane Care and Use of Laboratory Animals, Animal Welfare Act, and the Guide for the Care and Use of Laboratory Animals (44).

IVIS Imaging. Texas Red–labeled OVA and FITC-labeled CpG were used to track cargo in mouse skin. For all MN applications, the lower back of C57BL/6 mice were shaved and treated with Nair to remove hair. A MN patch was pressed onto the bare skin for 2 min using thumb pressure. For longer treatment up to 24 h, MN patches were secured with the adhesive portion of a Band-Aid followed by a layer of 3M Durapore high adhesion (silk) surgical tape. Mice were imaged with IVIS Lumina before or after MN applications at 2 min, 2, 24, 48, and 72 h. For 48 and 72 h time points, mice were only treated with MNs for 24 h. n = 4 mice at each time point for all groups. OVA–Texas Red was imaged at excitation: 570 nm, emission: Cy5.5; CpG-FITC was imaged at excitation: 465 nm, emission: GFP.

Flow Cytometry Analysis of dLNs. Mice (n = 4 for all groups) were treated with MN patches as described in the *IVIS Imaging* section. After euthanization at various time points, the draining inguinal lymph nodes were collected and dissociated into single-cell suspensions using frosted slides. Cells were counted, stained with fluorescently labeled antibodies (CD11c-PE, F4/80-APC, B220-eFluor450, PDCA-1-PE-Cy7, CD3-APC-eFluor780, and CD80-PE-Cy7), and analyzed on a Cyan flow cytometer with Summit software (Dako). GC B cells in dLNs were stained with B220-eFluor450, GL7-AlexaFluor647, and CD95-FITC on day 34 post–prime immunization.

Immunization Studies. Mice were immunized with coated MN patches loaded with 16.7 μg OVA and 2.5 μg CpG (n = 6) for 24 h and removed. Control groups included untreated (n = 6), blank MN (n = 3), SC (n = 9), and ID (n = 6) injection of OVA (16.7 μg) + CpG (2.5 μg) mix, SC 500 μg Alum (Alhydrogel, InVivogen) + 16.7 μg OVA (n = 6). All groups received two immunizations on day 0 and 23. Serum samples were collected on day 21, 30, 49, 119, 147, and 196 by submandibular bleeding for antibody analysis. For a dose-sparing study, MN patches loaded with various amount of OVA and CpG were applied for 24 h and removed in each immunization (n = 5 for all groups).

Evaluation of Vaccine-Induced Antibodies. OVA-specific antibody responses were evaluated by antigen-capture enzyme-linked immunosorbent assay (ELISA) in the immune sera. Briefly, OVA was coated on ELISA plates overnight at 4 °C. Plates were washed and incubated with serially diluted mouse immune sera for 2 h at room temperature. Bound antibodies were detected by HRP-conjugated anti-mouse IgG, IgG1, or IgG2a antibodies (1:3,000, Santa Cruz). Then, plates were developed using 3,3′,5,5′-Tetramethylbenzidine (eBioscience) for 10 min at room temperature, and the absorbance was measured at 450 and 570 nm. IgG titers were determined as the highest dilution that showed absorbance optical density$_{450-570}$ ($OD_{450-570}$) > 0.1.

IFN-γ ELISpot Assay. The frequency of antigen-specific IFN-γ–producing T cells was evaluated using the IFN-γ ELISpot Lit (BD Biosciences). Briefly, spleen cells were harvested from immunized mice on day 34 and restimulated with 10 μg/mL SIINFEKL peptide (100,000 splenocytes/well) for 17 h at 37 °C in Immobilon-P PVDF plates (Millipore) coated with anti-mouse IFN-γ antibody. Spots were developed following manufacturer's instructions.

Cytokine ELISA. On day 34, spleen cells (200,000/well) were restimulated with 20 μg/mL OVA for 68 h at 37 °C. Conditioned medium was evaluated for the secretion of cytokines and the secretion from $CD4^+$ T cells using mouse IFN-γ, TNF-α, IL-2, and IL-4 ELISA kits (BD) following manufacturer's protocol.

Statistics. Statistical analysis was performed using GraphPad Prism 8 software. Data are presented as mean ± SD. Unpaired Student's t tests were utilized to compare two groups, while one-way ANOVA with Tukey's or Kruskal–Wallis multiple comparisons tests were used to compare multiple groups. P values less than 0.05 were considered statistically significant.

Data Availability. All study data are included in the article and/or *SI Appendix*.

ACKNOWLEDGMENTS. This work was supported by the Defense Threat Reduction Agency (Award HDTRA1-13-1-0045), a Sponsored Research Agreement from Carbon, Inc., Stanford University Innovative Medicines Accelerator, and Joseph M. DeSimone Start-up Funds at Stanford University. We acknowledge the Chapel Hill Analytical and Nanofabrication Laboratory, a member of the North Carolina Research Triangle Nanotechnology Network that is supported by SF Grant ECCS-1542015 as part of the National Nanotechnology Coordinated Infrastructure.

1. P. M. Moyle, I. Toth, Modern subunit vaccines: Development, components, and research opportunities. *ChemMedChem* **8**, 360–376 (2013).
2. S. G. Reed, M. T. Orr, C. B. Fox, Key roles of adjuvants in modern vaccines. *Nat. Med.* **19**, 1597–1608 (2013).
3. Z. B. Wang, J. Xu, Better adjuvants for better vaccines: Progress in adjuvant delivery systems, modifications, and adjuvant-antigen codelivery. *Vaccines (Basel)* **8**, E128 (2020).
4. S. M. Gheibi Hayat, M. Darroudi, Nanovaccine: A novel approach in immunization. *J. Cell. Physiol.* **234**, 12530–12536 (2019).
5. R. Pati, M. Shevtsov, A. Sonawane, Nanoparticle vaccines against infectious diseases. *Front. Immunol.* **9**, 2224 (2018).
6. B. Pulendran, R. Ahmed, Immunological mechanisms of vaccination. *Nat. Immunol.* **12**, 509–517 (2011).
7. D. J. Irvine, A. Aung, M. Silva, Controlling timing and location in vaccines. *Adv. Drug Deliv. Rev.* **158**, 91–115 (2020).
8. S. N. Mueller, S. Tian, J. M. DeSimone, Rapid and persistent delivery of antigen by lymph node targeting PRINT nanoparticle vaccine carrier to promote humoral immunity. *Mol. Pharm.* **12**, 1356–1365 (2015).
9. S. W. Metz *et al.*, Precisely molded nanoparticle displaying DENV-E proteins induces robust serotype-specific neutralizing antibody responses. *PLoS Negl. Trop. Dis.* **10**, e0005071 (2016).
10. J. K. Hickling *et al.*, Intradermal delivery of vaccines: Potential benefits and current challenges. *Bull. World Health Organ.* **89**, 221–226 (2011).
11. J. Arya, M. R. Prausnitz, Microneedle patches for vaccination in developing countries. *J. Control. Release* **240**, 135–141 (2016).
12. M. B. Wilck *et al.*, Safety and immunogenicity of modified vaccinia Ankara (ACAM3000): Effect of dose and route of administration. *J. Infect. Dis.* **201**, 1361–1370 (2010).
13. B. G. Weniger, G. M. Glenn, Cutaneous vaccination: Antigen delivery into or onto the skin. *Vaccine* **31**, 3389–3391 (2013).

14. P. E. Laurent *et al*., Evaluation of the clinical performance of a new intradermal vaccine administration technique and associated delivery system. *Vaccine* **25**, 8833–8842 (2007).
15. E. Larrañeta, R. E. M. Lutton, A. D. Woolfson, R. F. Donnelly, Microneedle arrays as transdermal and intradermal drug delivery systems: Materials science, manufacture and commercial development. *Mater. Sci. Eng. Rep.* **104**, 1–32 (2016).
16. M. R. Prausnitz, Microneedles for transdermal drug delivery. *Adv. Drug Deliv. Rev.* **56**, 581–587 (2004).
17. Y.-C. Kim, J.-H. Park, M. R. Prausnitz, Microneedles for drug and vaccine delivery. *Adv. Drug Deliv. Rev.* **64**, 1547–1568 (2012).
18. H. S. Gill, M. R. Prausnitz, Coated microneedles for transdermal delivery. *J. Control. Release* **117**, 227–237 (2007).
19. R. S. J. Ingrole, H. S. Gill, Microneedle coating methods: A review with a perspective. *J. Pharmacol. Exp. Ther.* **370**, 555–569 (2019).
20. S. Kommareddy *et al*., Influenza subunit vaccine coated microneedle patches elicit comparable immune responses to intramuscular injection in guinea pigs. *Vaccine* **31**, 3435–3441 (2013).
21. C. L. Caudill, J. L. Perry, S. Tian, J. C. Luft, J. M. DeSimone, Spatially controlled coating of continuous liquid interface production microneedles for transdermal protein delivery. *J. Control. Release* **284**, 122–132 (2018).
22. A. V. Boopathy *et al*., Enhancing humoral immunity via sustained-release implantable microneedle patch vaccination. *Proc. Natl. Acad. Sci. U.S.A.* **116**, 16473–16478 (2019).
23. L. Y. Chu *et al*., Enhanced stability of inactivated influenza vaccine encapsulated in dissolving microneedle patches. *Pharm. Res.* **33**, 868–878 (2016).
24. P. C. DeMuth, Y. Min, D. J. Irvine, P. T. Hammond, Implantable silk composite microneedles for programmable vaccine release kinetics and enhanced immunogenicity in transcutaneous immunization. *Adv. Healthc. Mater.* **3**, 47–58 (2014).
25. J. W. Lee, J.-H. Park, M. R. Prausnitz, Dissolving microneedles for transdermal drug delivery. *Biomaterials* **29**, 2113–2124 (2008).
26. Z. Luo *et al*., Biodegradable gelatin methacryloyl microneedles for transdermal drug delivery. *Adv. Healthc. Mater.* **8**, e1801054 (2019).
27. N. G. Rouphael *et al*., The safety, immunogenicity, and acceptability of inactivated influenza vaccine delivered by microneedle patch (TIV-MNP 2015): A randomised, partly blinded, placebo-controlled, phase 1 trial. *Lancet* **390**, 649–658 (2017).
28. Y.-C. Kim *et al*., Enhanced memory responses to seasonal H1N1 influenza vaccination of the skin with the use of vaccine-coated microneedles. *J. Infect. Dis.* **201**, 190–198 (2010).
29. P. C. Demuth, W. F. Garcia-Beltran, M. L. Ai-Ling, P. T. Hammond, D. J. Irvine, Composite dissolving microneedles for coordinated control of antigen and adjuvant delivery kinetics in transcutaneous vaccination. *Adv. Funct. Mater.* **23**, 161–172 (2013).
30. D. Alizadeh *et al*., Induction of anti-glioma natural killer cell response following multiple low-dose intracerebral CpG therapy. *Clin. Cancer Res.* **16**, 3399–3408 (2010).
31. C. Edens, M. L. Collins, J. L. Goodson, P. A. Rota, M. R. Prausnitz, A microneedle patch containing measles vaccine is immunogenic in non-human primates. *Vaccine* **33**, 4712–4718 (2015).
32. M. J. Mistilis, A. S. Bommarius, M. R. Prausnitz, Development of a thermostable microneedle patch for influenza vaccination. *J. Pharm. Sci.* **104**, 740–749 (2015).
33. V. Bachy *et al*., Langerin negative dendritic cells promote potent CD8+ T-cell priming by skin delivery of live adenovirus vaccine microneedle arrays. *Proc. Natl. Acad. Sci. U.S.A.* **110**, 3041–3046 (2013).
34. C. Kolluru, Y. Gomaa, M. R. Prausnitz, Development of a thermostable microneedle patch for polio vaccination. *Drug Deliv. Transl. Res.* **9**, 192–203 (2019).
35. A. R. Johnson *et al*., Single-step fabrication of computationally designed microneedles by continuous liquid interface production. *PLoS One* **11**, e0162518 (2016).
36. P. Marrack, A. S. McKee, M. W. Munks, Towards an understanding of the adjuvant action of aluminium. *Nat. Rev. Immunol.* **9**, 287–293 (2009).
37. H. Shirota, D. M. Klinman, Recent progress concerning CpG DNA and its use as a vaccine adjuvant. *Expert Rev. Vaccines* **13**, 299–312 (2014).
38. E. Panagioti, P. Klenerman, L. N. Lee, S. H. van der Burg, R. Arens, Features of effective T cell-inducing vaccines against chronic viral infections. *Front. Immunol.* **9**, 276 (2018).
39. E. Kim *et al*., Microneedle array delivered recombinant coronavirus vaccines: Immunogenicity and rapid translational development. *EBioMedicine* **55**, 102743 (2020).
40. S. Awate, L. A. Babiuk, G. Mutwiri, Mechanisms of action of adjuvants. *Front. Immunol.* **4**, 114 (2013).
41. S. Jackson *et al*., Immunogenicity of a two-dose investigational hepatitis B vaccine, HBsAg-1018, using a Toll-like receptor 9 agonist adjuvant compared with a licensed hepatitis B vaccine in adults. *Vaccine* **36**, 668–674 (2018).
42. J. Scheiermann, D. M. Klinman, Clinical evaluation of CpG oligonucleotides as adjuvants for vaccines targeting infectious diseases and cancer. *Vaccine* **32**, 6377–6389 (2014).
43. A. Vrdoljak *et al*., Induction of broad immunity by thermostabilised vaccines incorporated in dissolvable microneedles using novel fabrication methods. *J. Control. Release* **225**, 192–204 (2016).
44. National Research Council, *Guide for the Care and Use of Laboratory Animals* (National Academies Press, Washington, DC, ed. 8, 2011).